ELSEVIER

International Journal of Mass Spectrometry 212 (2001) 13–23

International Journal of Mass Spectrometry

www.elsevier.com/locate/ijms

Instrumentation

Design of a new electrospray ion mobility mass spectrometer

Thomas Wyttenbach, Paul R. Kemper, Michael T. Bowers*

Department of Chemistry and Biochemistry, University of California at Santa Barbara, Santa Barbara, CA 93106-9510, USA

Received 7 May 2001; accepted 14 July 2001

Abstract

The design of a new ion mobility mass spectrometer is presented. The design features an electrospray ion source; an ion funnel to transmit ions efficiently from the source to the mobility cell and to accumulate ions in the pulsed ion mode; a mobility cell, and a quadrupole mass analyzer. Each part of the instrument is described in detail. Preliminary results obtained with the new instrument are presented to demonstrate its capabilities. Equilibrium experiments showed that the $\Delta G°$(300 K) values for the addition of the first water molecule to the doubly protonated peptides bradykinin, angiotensin II, and LHRH are in the range from -3.5 to -2.5 kcal/mol. The corresponding values for the singly protonated ions are >-0.5 kcal/mol for angiotensin II and LHRH, but equal to -2.6 kcal/mol for bradykinin. The stronger bonding in bradykinin may be due to the presence of a salt bridge structure. Ion arrival time distributions showed that singly protonated peptides can form aggregates of the form $(n\mathrm{M} + n\mathrm{H})^{n+}$. The mobilities of these ions indicated that they are near spherical. Heating the drift cell to ~450 K caused dissociation of the $(2\mathrm{M} + 2\mathrm{H})^{2+}$ ion into two $(\mathrm{M} + \mathrm{H})^{+}$ units on the 1 ms experimental time scale. A theoretical fit to the experimental data yielded rate constants and a barrier for dissociation of 30 ± 2 kcal/mol for bradykinin and 39 ± 3 kcal/mol for LHRH. (Int J Mass Spectrom 212 (2001) 13–23) © 2001 Elsevier Science B.V.

Keywords:

1. Introduction

Electrospray ionization has become an essential tool in biological mass spectrometry. Further, when electrospray is coupled with ion mobility measurement [1,2] additional important information on molecular conformation can be obtained as shown in recent work by Jarrold and co-workers [3–6] and Clemmer and co-workers. [7,8] For example, it was found in several cases that the low positive charge states of proteins adopt a very compact conformation in the gas phase, even more compact than the crystal structure [4]. This effect was attributed to the absence of a surrounding media, which tends to pull the structure apart. The higher charge states, on the other hand, are more extended and approach a stretched out conformation as additional protons are added (due to coulomb repulsion). For charge states between the

* Corresponding author. E-mail: bowers@chem.ucsb.ed

Dedicated to R. Graham Cooks on the occasion of his sixtieth birthday.

PII S1387-3806(01)00517-6

two extremes, several distinct conformations between folded and unfolded are often detected [4,7] and temperature dependent studies allow examination of the unfolding process [7,9]. For model systems the presence or absence of secondary [5,6] and tertiary [8,10] structure was studied leading to the first intrinsic helix propensity scale for some of the common amino acids [11].

Although important information can be obtained from solvent free gas phase measurements and calculations, it is very clear that connecting this information to solution studies is of critical importance. Work on this objective has begun in several laboratories both on real biological systems [12,13] and on model systems [14–16], and sequential binding energies for individual water molecule additions have been measured for small peptides [14] and proteins [12,17]. For small systems with exposed charges $\Delta G°(\sim 300K)$ values for the addition of the first water molecule are as large as -10 kcal/mol [14], whereas free energy changes for the successive water molecules are less negative. For larger systems (such as proteins) on the other hand, $\Delta G°$ values of hydration are of the order of -4 kcal/mol and depend on the degree of protein folding [12]. These hydration measurements can also provide important structural information. For instance the protein BPTI was found to have a special site for the first water molecule addition [17,18]. And, in a different approach, the abundance of hydrated ions $X^+(H_2O)_n$ was measured as a function of n. Significant differences between folded and unfolded species and in some cases magic numbers for certain values of n were found in these experiments [13,15,16].

In this article we describe the design of a new ion mobility mass spectrometer. It was designed to probe both the structural changes and energetics associated with sequential solvation of biopolymers. Ideally, this solvation will extend from the gas phase to solution. We will demonstrate that the new instrument can indeed be employed to study both the intrinsic properties of the solvent-free biomolecules and their solvation. The scientific results reported here are considered preliminary and in-depth studies will be published elsewhere.

2. Instrumentation

The electrospray ion mobility mass spectrometer is set up on a steel frame cart that holds the vacuum chambers and two diffusion pumps. A cross-sectional view of the stainless steel vacuum chambers and their interior is shown in Fig. 1. The 12 in. o.d. main chamber (a) contains the ion mobility cell (f) and is pumped by a 10 in. diffusion pump (Edwards, Sussex, England, 2000 L/s). A 6 in. o.d. detector chamber (b) is pumped by a 6 in. diffusion pump (Edwards, Sussex, England, 700 L/s). The electrospray source is isolated from the main chamber by two stages of differential pumping using two mechanical pumps (E2M40, Edwards, Sussex, England) attached to the two elbows (c) on the source flange (d).

Ions are sprayed from an external needle (not shown) and enter the vacuum system through a capillary that feeds the ion funnel (e). The ions are funneled and guided through two stages of differential pumping and subsequently injected into the drift cell (f). Ions that exit the cell are mass selected in the quadrupole mass analyzer (g) and finally counted with a conversion dynode/CEM detection system (h and i). A more thorough description of the different components of the apparatus is given in the following sections.

2.1. Electrospray

The elctrospray source consists of two major components: the needle containing the electrospray solution and the capillary that acts as the vacuum interface. Both metalized glass needles (PicoTip, New Objective, Cambridge, MA, 1.2 mm o.d., 2 μm tip) and hypodermic stainless steel needles (0.004 in. o.d., $\sim$70 μm i.d.) glued into stainless steel tubes (1/16 in. o.d. $\times$ 0.010 in. i.d.) are used as spray tips. The needle is mounted on an x, y, z translation stage. The glass needles serve as nanospray tips (the needle is the liquid reservoir) and are typically operated without any backpressure. The hypodermic needles are fed by a syringe pump with typical flow rates of 20–50 μL/h. Nanospray appears to be ideal for quick experiments and for peptide work whereas the syringe pump setup appears to be the method of choice for proteins. The

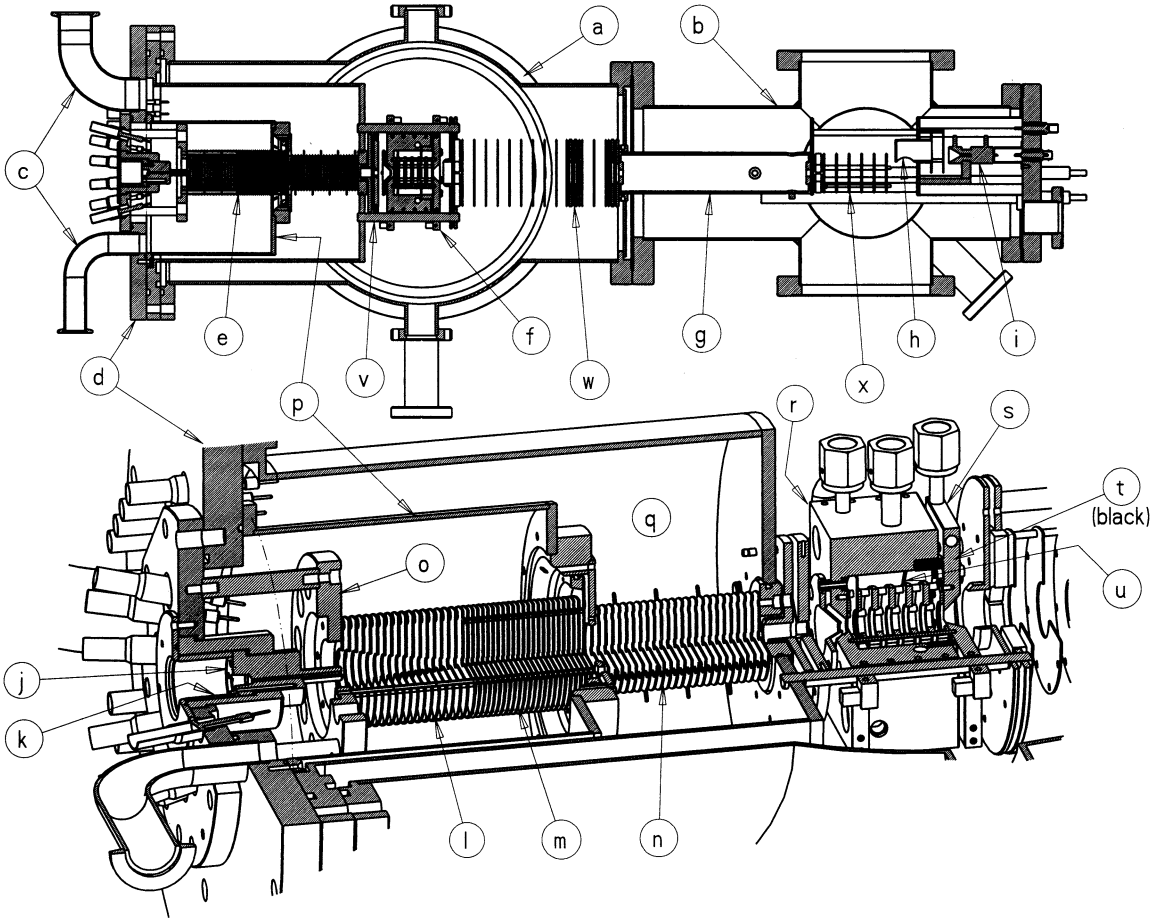

Fig. 1. (Top) Cross-sectional view of entire instrument as viewed from the top. (Bottom) Perspective cross-sectional view of source, funnel, and cell. (a) and (b) vacuum chambers, (c) pump ports, (d) source flange, (e) ion funnel, (f) drift cell, (g) quadrupole mass analyzer, (h) conversion dynode, (i) detector, (j) capillary heating block, (k) insulator, (l) funnel first section, (m) funnel second section, (n) funnel third section, (o) funnel flange, (p) hat flange, (q) second pump stage, (r) cell body, (s) cell end cap, (t) ceramic ring, (u) guard rings, and (v), (w), (x) ion optics.

high voltage on the spray needle is typically +500–2000 V with respect to the capillary for nanospray and ~2 kV for positive ion electrospray. The capillary (0.010 in. i.d.) is 3.0 in. long and is inserted into an aluminum block (j), which can be heated to 250 °C. The aluminum block is mounted to a heat resistant PEEK insulator (k), which is in turn mounted to the source flange (d).

2.2. Ion funnel

The ion funnel is the interface between the electrospray ionization (ESI) source and the ion drift cell located in the high vacuum chamber. It is a high transmission rf ion guide device that has two functions: First, it compresses the divergent stream of ions leaving the capillary down to a small diameter. Second, it can move the ions from the source region to the drift cell without the use of high acceleration fields, thus avoiding high-energy ion–neutral collisions.

Our ion funnel was modeled after the original designs of Smith and co-workers [19]. In our design there are three individually tunable sections (l, m, and n in Fig. 1). The first two sections are stacks of 18 and

24 lenses (0.030 in. thick, 2.00 in. o.d.), respectively. The lens holes in the first stack decrease parabolically from 0.87 to 0.14 in. diameter; those in the second stack decrease down to 0.10 in. diameter. The third section consists of 25 lenses (0.030 in. thick, 1.60 in. o.d., 0.16 in. i.d.). The lenses in the first two sections are stacked on six ceramic tubes and mounted on the funnel entrance side to a plastic flange (o). Flange (o) is mounted to the source flange (d) allowing easy removal for cleaning.

The first 18 lenses in the funnel (with the largest orifices) are spaced apart 0.100 in. using ceramic spacers. These lens hole diameters are nearly identical with those reported in ref. [19]. As the lens orifice diameter decreases to a value comparable to the lens spacing, however, our trajectory calculations carried out using SIMION [20] indicated that ion transmission drops sharply. In other words, the funnel works best when the space between the lenses is smaller than the lens orifices. Also, the orifice size must be larger than the lens thickness to avoid a field free region inside the lens. These effects were found independently in Smith's lab as well [21]. With this in mind, we decided to stack the lenses in section two (m) closer together and to avoid small orifice diameters altogether. Both of these goals were achieved by using 1/16 in. thick "O" rings to space lenses 18 through 42. Since the orifices of lenses 19 through 26 decrease linearly from 0.14 in. to 0.10 in. whereas lenses 27 through 42 all have 0.100 in. diameter orifices, the orifice diameters are always greater than the lens spacing of 0.06 in. The "O" ring spacers not only provide closer lens spacing but also prevent radial pumping of gas out of the lens stack. This second effect has two consequences. First, conductance of the viscous gas flow into the next pumping stage (q) is greatly reduced because the flow is through a quasitube rather than a single orifice. Second, the ions are embedded in a directed flow of gas into the next pumping stage, which should increase ion transmission.

The final section of the funnel (n) is mounted to the hat flange (p) and is located in the next pumping stage (q). The first 16 lenses are again spaced by 0.100 in. ceramic spacers, whereas the last 9 are spaced by 3/32 in. "O" rings to decrease the pumping conductance into the following chamber.

The effect of pressure on the funnel operation is somewhat uncertain. Previous reports [19,21] and our SIMION modeling both indicate that collisions are important in constraining the ions to the center of the funnel and reducing their kinetic energy. In the present instrument, the funnel operates in two pressure zones: the pressure in sections 1 and 2 (directly after the capillary) is ~0.2 Torr; section 3 is ~0.02 Torr. Efficient ion trapping clearly occurs in both sections, thus we can say that pressures between 0.02 and 0.2 Torr are adequate for funnel operation. Increasing the pressure in the first sections (above 0.2 Torr) with N_2 did not improve the funnel performance.

Three 1 MHz rf generators with individually adjustable amplitudes are used for the three sections of the ion funnel. For each section two outputs are provided, 180° phase shifted from each other. In addition, three individually controllable dc drift voltages are provided as well, the voltage of each section floating on top of the previous section's potential. The appropriate drift voltage is applied to the first and last lens of each section, with the individual lenses being fed by a 1 MΩ resistor chain. The rf is applied to the lenses by way of 1000 pF capacitors, alternating the (+) and (−) outputs. The last two lenses in the funnel are independently tunable focusing lenses and do not carry any rf.

The dc applied to section one (2.23 in. long) is typically 10–50 V, the peak-to-peak rf voltage 100–200 V. The corresponding values for section two (2.26 in. long) are 30–50 V dc and 100–200 V rf and for section three (3.11 in. long) 1–5 V dc and 50–150 V rf. The voltage between the last lens of section three and the drift cell entrance orifice determines the ion injection energy. It is adjustable from 0 to 200 V and is typically 20–60 V. Higher injection energies can be used to effect structural changes and/or fragmentation of the ions, if desired.

The next to the last lens in the funnel can be pulsed to gate the continuous ion beam from the ESI source. A voltage high enough to stop the beam is applied to close the gate. Because ions cannot readily escape

radially due to the rf trapping nor can they exit back into the source due to the dc ramp applied, they accumulate near the exit of the ion funnel. The gate is opened by pulsing the lens potential down to the normal voltage for approximately 10 μs. For cell drift times in the range from 100 μs to 1 ms a pulsing repetition rate of 1-–10 kHz is typically used. The number of ions per second counted after the quadrupole mass filter is approximately the same in continuous and pulsed ion beam mode, indicating a near 100% trapping efficiency in the ion funnel.

2.3. Drift cell

The drift cell used in this experiment is very similar to those described previously [22]. It consists of a near cubic copper body (3.5×3.5×2.0 in., r in Fig. 1), that can be heated by electrical heaters and cooled with a flow of liquid nitrogen, a copper end cap (s) with separate temperature control, and a ceramic ring (t) that separates the end cap from the body. The drift field in the cylindrical interior of the cell body is created by the entrance and exit plates (0.005 in. thick, 0.5 mm orifice) held in place by guard rings at the same potential (0.057 in. thick, 0.600 in. i.d.) and by four intermediate guard rings (u, 0.115 in. thick, 0.600 in. i.d.) equally spaced and mounted on six ceramic rods. A precision 1 MΩ resistor chain connects the rings. The total drift length from entrance to exit plate is 4.503 ± 0.002 cm. The cell temperature is variable from 80 to above 800 K.

Typical operating pressures are 4–5 Torr with drift voltages ranging from 2 to 20 V/cm yielding conditions within the low field limit [23]. Higher pressures and voltages (up to 1000 V across the cell) are possible, however this requires smaller cell orifice holes.

2.4. Mass analyzer and detector

Ions exiting the drift cell enter a 0–4000 u quadrupole mass filter (g, ABB Extrel, Pittsburgh, PA) followed by an off-axis conversion dynode (h). Particles leaving the conversion dynode are detected by a channel electron multiplier (i, K&M Electronics, West Springfield MA). The TTL signal pulses from the preamp are collected with a multichannel scaler board (MCSplus, EG&G Ortec, Oak Ridge, TN). The MCS is equipped with a voltage ramp generator, which is used to scan the quadrupole mass analyzer.

2.5. Electronics

The electronic units necessary to control the ESI source, the ion funnel, the drift cell, and the ion optics (v, Fig. 1) in front of the drift cell (three lenses plus *x/y* steering), (w) in front of the quadrupole (three lenses plus *x/y* steering), and (x) in front of the detector (two lenses plus *x/y* steering) were built in-house. The quadrupole mass filter employed here cannot be floated significantly and was thus fixed at ground potential. The voltage on the drift cell exit orifice then determines the ion energy along the quadrupole axis; the cell entrance voltage floats on top of the exit orifice potential and determines the drift potential; the end of the ion funnel floats on the cell entrance potential and determines the ion injection energy. Similarly, the three sections of the ion funnel float on top of each other and the ESI capillary on top of the funnel. The electrospray needle is the last element and is referenced to the capillary. This stacking arrangement is necessary since any change in voltage in the series (in the cell drift potential, for example) must be tracked by all the preceding potentials to maintain a constant ion formation and injection environment. If the individual lens supplies were individually referenced to ground, any change in one lens would require resetting all previous lens voltages.

The potentially high voltages in the ion funnel with respect to ground and the relatively high pressure in the ion funnel make the system prone to discharging. To avoid discharges no grounded metal parts are present inside the ion funnel vacuum chamber and the vacuum flange, support rods, and the support flange for the ion funnel were made of plastic.

3. Experimental

All samples were purchased from Sigma (St. Louis, MO) and used without further purification. The

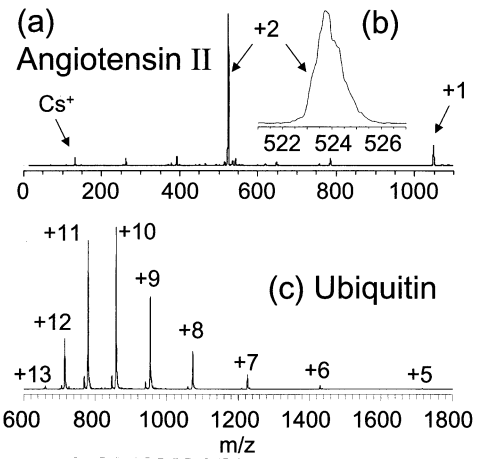

Fig. 2. (a) Mass spectrum of a mixture of CsI and angiotensin II; (b) blow-up of the peak at 524 u; (c) mass spectrum of ubiquitin.

spray solvent was a 1:1 mixture of acetonitrile and water acidified with trifluoroacetic acid to a concentration of 0.1%. The biomolecule samples were dissolved to a concentration of ~0.5 mM, CsI to ~2 mM. Peptides and CsI were sprayed from coated glass tips, ubiquitin from hypodermic needles. The helium pressure in the drift cell was ~5 Torr for quantitative ion mobility measurements and 3–5 Torr for the other experiments. The instrument was tuned to typical values as outlined in Sec. 2 unless otherwise mentioned.

4. Results

4.1. Mass spectra and ion currents

For peptides most of the signal results from the doubly (and sometimes triply) protonated peptide ions. Fig. 2(a) shows a mass spectrum of angiotensin II, a peptide with 8 residues. Here a solution of ~0.5 mM angiotensin II and ~2 mM CsI was sprayed. The $(M + 2H)^{2+}$ ion of angiotensin II is clearly the most abundant ion. For proteins a broad charge state distribution is observed with maximum intensity around $m/z = 1000$ [Fig. 2(c)] as is typical for ESI mass spectrometry.

The ion signal detected after the quadrupole in rf-only mode is typically 10^5 counts/s for peptides and $\geq 10^6$ counts/sec for proteins. Ion mobility theory [23] indicates that ~4% of ions are transmitted through the cell used here (under typical operating conditions), indicating that an ion current of ~1 pA enters the cell in the case of peptides (doubly charged) and perhaps one or two orders of magnitude more for proteins. The total ion current measured with an electrometer on the ion funnel is typically 100–300 pA. However, at this point most of the charge may be carried by small mass solvent ions, which are not of interest here and which are not efficiently transmitted through the ion funnel [19,21]. Poor transmission for small ions is predicted by theory [21], and is supported by the fact that we do not observe ions below mass 100 (e.g. solvated or naked H_3O^+ or Na^+ ions). However, from the spectrum shown in Fig. 2(a) it is apparent that Cs^+ ions ($m/z = 133$) are transmitted through the funnel at least with sufficient efficiency to be detected.

The insert in Fig. 2(b) is a blow-up of the peak at $m/z \sim 524$, corresponding to the $(M + 2H)^{2+}$ angiotensin II ion. The visible but unresolved C^{13} isotope distribution suggests a mass resolution $m/\Delta m_{10\%}$ of ~350. This resolution is near the maximum for the instrument but is similar to the resolution used in the experiments discussed in the following.

4.2. Equilibrium experiments

The present experimental setup is ideal for carrying out equilibrium experiments. First, the continuous ion beam ESI source provides greater intensity relative to pulsed sources such as matrix-assisted laser desorption ionization (MALDI); second, a drift cell that can be heated and cooled is required to determine 0 K bond dissociation energies; and third, a short cell with less ion loss is favored over longer cells. The presence of equilibrium can be easily demonstrated by changing the drift voltage (reaction time), which does not affect the observed mass spectra if equilibrium is established. The following studies of peptide hydration demonstrate nicely the capabilities of the instrument.

In the first experiment, the protonated peptide ions were injected (>100 eV [24]) into the drift cell, which

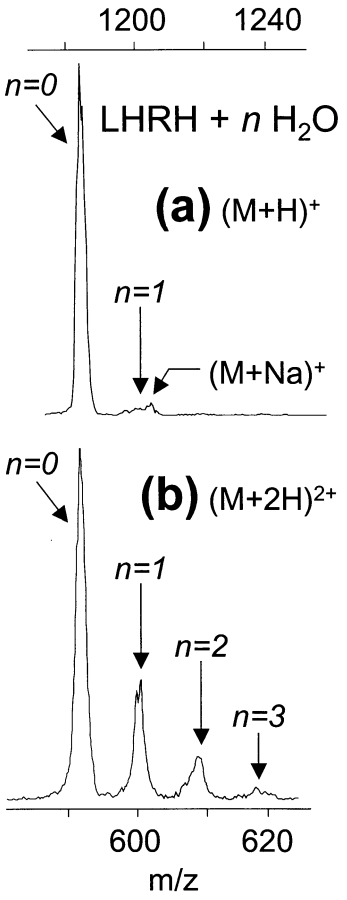

Fig. 3. Mass spectra of (a) singly and (b) doubly protonated LHRH exposed to ~1.5 Torr of water vapor in the drift cell at 300 K. "*n*" indicates the number of water molecules picked up by the peptide.

was filled with helium mixed with water vapor. Mass spectra obtained of LHRH ions exiting the cell filled with ~1.5 Torr H_2O are shown in Fig. 3. It is apparent that singly charged ions $(M + H)^+$ do not hydrate as fully as the doubly charged ions $(M + 2H)^{2+}$. Knowing the water pressure and cell temperature, we can calculate equilibrium constants and free energies of hydration from the relative peak intensities (Table 1).

In addition to the striking difference between $(M + H)^+$ and $(M + 2H)^{2+}$ systems there are also differences between different peptides. Singly protonated LHRH $(M + H)^+$ absorbs significantly less water than singly protonated bradykinin. This may reflect a difference in structure. Specifically, unsolvated bradykinin $(M + H)^+$ is believed to be a zwitterion with two protonated arginine residues and a deprotonated C-terminus [25–27], whereas LHRH has no acidic hydrogens and therefore cannot be a zwitterion. Further, molecular modeling studies indicate that the protonated site in LHRH $(M + H)^+$ is buried deep in the interior of the peptide and is well self-solvated [28]. Thus addition of a water solvent molecule only minimally increases charge solvation. In the case of a zwitterion, however, addition of water molecules is expected to substantially stabilize the charges, as the bradykinin peptide is not large enough to fully self-solvate two positive and one negative charge [26,28]. These effects may explain the observed differences in bradykinin and LHRH hydration. Extending this line of reasoning, the small free energy of hydration of singly charged angiotensin II (Table 1) suggests that this $(M + H)^+$ ion does not form a zwitterion, although angiotensin II is a potential candidate for zwitterion formation having three basic and two acidic sites. However, there is only one arginine among the basic residues as opposed to bradykinin, which has two; this could very well be responsible for the difference in hydration between the two peptides.

In larger protein systems, different effects are important. Here substantially more waters add to the lower charge states of proteins compared to medium and higher charge states and the amount of water pickup reaches a minimum for medium charge states (e.g. +10 for cytochrome *c*) [13]. Molecular model-

Table 1
Free energy of hydration at 302 K for the peptides bradykinin (BK), LHRH, and angiotensin II (AII) for the charge states +1 and +2; ΔG_n° refers to the addition of one H_2O molecule to the species with $(n - 1)$ H_2O molecules already bound

	ΔG_1° (kcal/mol)	ΔG_2° (kcal/mol)	ΔG_3° (kcal/mol)
BK (+1)	−2.6		
BK (+2)	−3.4	−3.0	N/A[a]
LHRH (+1)	>−0.5		
LHRH (+2)	−3.0	−2.3	−1.5
AII (+1)	−0.3		
AII (+2)	−2.6	−1.6	−1.8

[a]Too weak to measure.

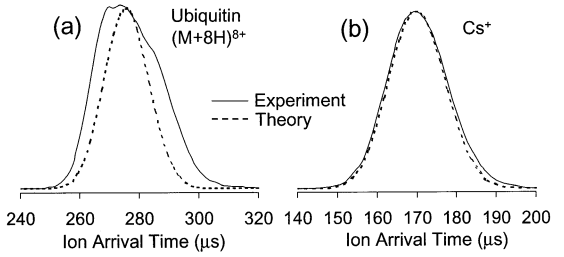

Fig. 4. Arrival time distributions of (a) ubiquitin charge state +8 and (b) Cs^+. The dashed line is the theoretically expected distribution assuming that all ions have the same collision cross section.

ing studies indicate that protein molecules are large enough to fully self-solvate the low to medium charge states [29]. On the other hand, the three-dimensional shape changes dramatically in proteins as a function of charge state from folded for lower charge states to unfolded for the higher charge states. The protein studies also indicate that the degree of water addition is directly correlated with the degree of folding for the lower charge states [13]. Thus the water molecules appear to find better binding sites with multiple coordination in the folded protein even though direct solvation of the charge is not possible. These favored sites decrease as the protein unfolds, reducing the water uptake. In the highest charge states, the charges are not fully solvated by the protein and water uptake begins to increase indicating that direct solvation of the charges is probably occurring.

The room temperature $\Delta G°$ values of hydration shown in Table 1 will be extended to higher and lower temperatures in the near future. This will allow bond enthalpies $\Delta H°$ and entropies $\Delta S°$ to be determined.

4.3. Ion mobility experiments

Ion mobilities are measured by recording the arrival time distribution (ATD) of a pulse of ions that drifts through the cell filled with pure helium. Fig. 4(a) shows the ATD of a ubiquitin $(M + 8H)^{8+}$ ion pulse that was ~10 μs wide at the entrance of the cell. The peak observed is significantly broader than 10 μs due to diffusion in the drift cell and to multiple overlapping features resulting from different conformations with different cross sections. The expected width of a single feature, calculated theoretically using the transport equation for ions in the drift tube, [23] is shown by the dashed line in Fig. 4(a). It is substantially broader than the original 10 μs due to diffusion, but is also clearly narrower than the experimental width, confirming the presence of more than one feature. Fig. 4(b) shows the experimental and theoretical ATD of Cs^+. In this case theory and experiment match very well confirming the absence of multiple features. The top panel of Fig. 5 shows the ATD of the +7 charge state of ubiquitin. The major peak lines up with and has about the same width as the +8 charge state peak in Fig. 4(a), but there is a shoulder at shorter times. This shoulder is obviously due to ions that are more compact and drift faster than the ions comprising the major peak. The shoulder becomes the major peak in the +6 charge state at low injection energies (Fig. 5) and there is clear evidence for a third feature due to even more compact ions. By increasing the ion injection energy the $(M + 6H)^{6+}$ peaks at short times disappear and the intensity shifts to the peak at longest times which correlates with the major peaks observed for $(M + 8H)^{8+}$ and $(M + 7H)^{7+}$. In this higher energy experiment the compact

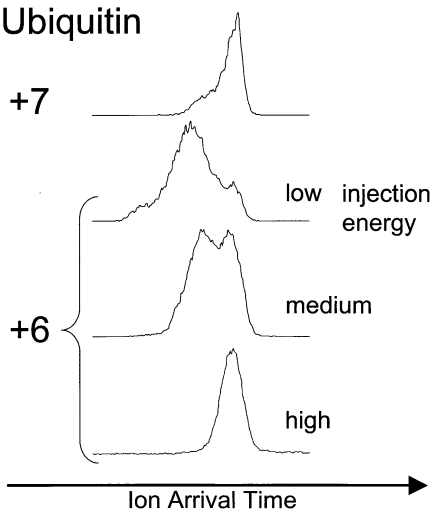

Fig. 5. Arrival time distributions of ubiquitin charge states +6 and +7. The compact +6 structures at short times are annealed to open structures at longer times when the injection energy is increased.

$(M + 6H)^{6+}$ ions are annealed to more open conformations by collisions with helium at the entrance to the drift cell (Fig. 5). Similar ATDs have been reported previously for ubiquitin [7] and other proteins [4] and the three features seen for ubiquitin have been assigned as compact, partially folded, and unfolded conformations [7]. Thus, the measurement of ATDs can be a powerful aid in obtaining structural information for complicated molecular systems.

When the drift voltage is lowered (at constant pressure), ions spend more time in the drift cell, the ATD peak shifts to longer times, and the peak becomes broader. Plotting the average arrival time versus the ratio of pressure to drift voltage yields a straight line. The low field ion mobility (K_0) can be obtained from the slope. (The intercept is the time of flight outside the drift cell.) In the case of Cs^+ the resulting K_0 is 18.5±0.5 $cm^2\,V^{-1}\,s^{-1}$ (extrapolated to 0 V injection energy). The value of K_0 compares well with the literature value of 18.3 ± 0.3 $cm^2\,V^{-1}\,s^{-1}$ [30] and with values previously measured with our MALDI experiment (18.3 ± 0.5 $cm^2\,V^{-1}\,s^{-1}$) [31]. Because of ion penetration effects in the present ESI setup, the apparent K_0 is slightly dependent on the injection energy (rising to 18.8 $cm^2\,V^{-1}\,s^{-1}$ at 20 V injection, 5.2 Torr of He). However, this injection effect is not generally observed for the peptide ions due to their much larger cross sections. For bradykinin $(M + 2H)^{2+}$ we measure a K_0 of 4.36 ± 0.08 $cm^2\,V^{-1}\,s^{-1}$, in agreement with the value of 4.42 $cm^2\,V^{-1}\,s^{-1}$ [32] previously reported.

The ATD of singly charged bradykinin $(M + H)^+$ shows a second feature that we believe is due to the $(2M + 2H)^{2+}$ ion which also has $m/z = 1061$, identical to $(M + H)^+$. Formation of aggregates of $(M + H)^+$ units in ESI mass spectrometry is not unique to bradykinin, but rather appears to be a general property of peptides. We have observed aggregates for all the peptides we have looked at: bradykinin, angiotensin II (LHRH), and neurotensin. Others have seen it for a number of other peptides [32,33]. It is striking, though, that aggregates $(xM + yH)^{y+}$ where $x = y$ are by far the most abundant clusters. We have found no evidence for the existence of any $x \neq y$ clusters,

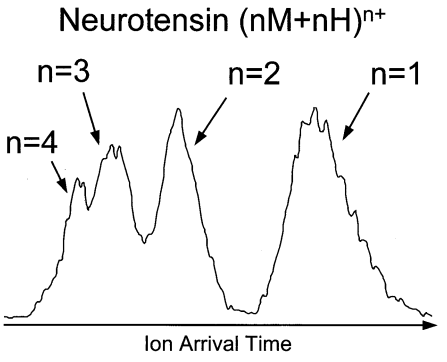

Fig. 6. Arrival time distribution of mass selected ($m/z = 1674$) neurotensin ions. The various features correspond to aggregates of protonated neurotensin units of the form $(nM + nH)^{n+}$.

although the possible formation of $(2M + 3H)^{3+}$ of bradykinin has been reported elsewhere [32].

Fig. 6 shows an example of these multiple features in the ATD of neurotensin. Here, the quadrupole was set at $m/z = 1674$ [corresponding to $(nM + nH)^{+n}$] and the four resolved features seen in Fig. 6 correspond to $n = 1$–4. The feature at longest drift times corresponds to the monomer $(M + H)^+$. Doubly charged ions with the same cross-section drift twice as fast in a given electric field as the singly charged ion. However, the doubly charged dimer $(2M + 2H)^{2+}$ has a larger collision cross section than the monomer, which slows it down. The ratio of cross sections is $2^{2/3}$ if both the monomer and the dimer are spherical. Thus we might expect the mobilities of these clusters to increase as $n^{1/3}$. The relative mobilities of the four resolved features seen in Fig. 6 are 1.00, 1.24, 1.43, and 1.56, in very close agreement with the $n^{1/3}$ dependence expected for spherical ions implying that all of these aggregates are nearly spherical. Similar results were obtained for the other peptides measured here.

Spraying a mixture of bradykinin (M_1) and LHRH (M_2) yields a mass spectrum similar to the superposition of the two individual spectra, but in addition a peak at $m/z = 1122$ is observed due to the mixed dimer. The ATD for $m/z = 1122$ is narrow, indicating that only a single component is present. The mobility obtained indicates that the species is $(M_1 + M_2 +$

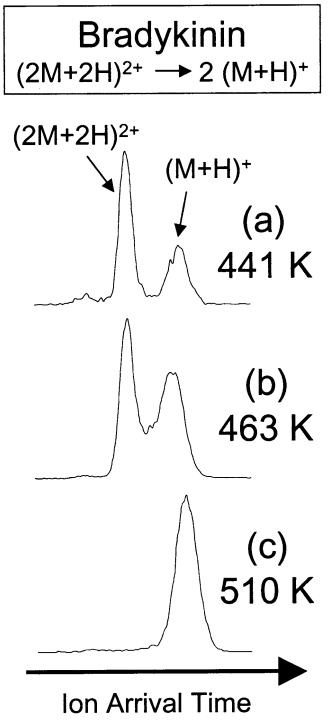

Fig. 7. Arrival time distributions measured for bradykinin at different cell temperatures. The dimer present at lower temperatures dissociates into two monomer units as the temperature is raised.

$2H)^{2+}$. There is no evidence for the formation of the singly charged $(M_1 + M_2 + H)^+$ species.

Raising the cell temperature allows the dissociation of $(nM + nH)^{n+}$ aggregates to be studied under controlled thermal conditions. Specifically, we recorded ATDs of the bradykinin and LHRH $(nM + nH)^{n+}$ ions as a function of cell temperature. On the experimental time scale of ~1 ms LHRH $(2M + 2H)^{2+}$ dissociates almost completely into two $(M + H)^+$ ions at 460 K, whereas bradykinin requires 510 K (Fig. 7). Onset for dissociation is observed at 410 K for LHRH and 440 K for bradykinin. The ATD obtained for bradykinin at 463 K is shown in Fig. 7(b). It can be seen that the features $(2M + 2H)^{2+}$ and $(M + H)^+$ are no longer baseline resolved, indicating some ions start out as $(2M + 2H)^{2+}$ ions and dissociate into two $(M + H)^+$ ions while in the drift field. This causes a fill-in between the peaks. For a given reaction rate coefficient, k, the amount of fill-in can be calculated using the ion transport equations for reactive species [34]. Thus, k can be obtained by a fit of the theoretical ATD to experiment [35]. By measuring k in this fashion, as a function of temperature, and using an Arrhenius type of analysis we arrive at a barrier for dissociation of 30 ± 2 kcal/mol for bradykinin and 39 ± 3 kcal/mol for LHRH. The corresponding pre-exponential factors are extremely high, 10^{17} and 10^{23} s^{-1}, respectively, indicating a very loose transition state and probably no reverse activation barrier. The fact that two LHRH $(M + H)^+$ ions are bound more strongly than bradykinin is somewhat surprising. A zwitterion structure, as is expected to occur in bradykinin, should intuitively lead to stronger bonds than the aggregation of two positive charge solvation structures, as found in LHRH. Clearly, more work has to be done to understand the nature of this interesting type of bonding.

5. Conclusions

We have introduced a new electrospray ion mobility mass spectrometer that uses an ion funnel as the interface between source and drift cell. The ion funnel is responsible for transmitting ions efficiently to the cell and efficiently storing ions in pulsed experiments. We have demonstrated the capabilities of the new instrument in a number of possible applications including thermodynamics of solvation, especially the hydration of peptides, structural analysis of large biomolecules, absolute ion mobilities, allowing comparison with theoretical structures, reaction rate coefficients measurements at different temperatures, allowing barriers and endothermicities to be determined.

Acknowledgments

The authors wish to thank the National Science Foundation under grant no. 9729146 for support of this research. They also thank Dr. Richard Smith for useful conversations during the design of the ion funnel interface.

References

[1] G.v. Helden, M.-T. Hsu, P.R. Kemper, M.T. Bowers, J. Chem. Phys. 95 (1991) 3835.
[2] D.E. Clemmer, M.F. Jarrold, J. Mass Spectrom. 32 (1997) 577.
[3] D.E. Clemmer, R.R. Hudgins, M.F. Jarrold, J. Am. Chem. Soc. 117 (1995) 10141.
[4] K.B. Shelimov, D.E. Clemmer, R.R. Hudgins, M.F. Jarrold, J. Am. Chem. Soc. 119 (1997) 2240.
[5] R.R. Hudgins, M.A. Ratner, M.F. Jarrold, J. Am. Chem. Soc. 120 (1998) 12974.
[6] M. Kohtani, B.S. Kinnear, M.F. Jarrold, J. Am. Chem. Soc. 122 (2000) 12377.
[7] J. Li, J.A. Taraszka, A.E. Counterman, D.E. Clemmer, Int. J. Mass Spectrom. 185 (1999) 37.
[8] A.E. Counterman, D.E. Clemmer, J. Am. Chem. Soc. 123 (2001) 1490.
[9] Y. Mao, J. Woenckhaus, J. Kolafa, M.A. Ratner, M.F. Jarrold, J. Am. Chem. Soc. 121 (1999) 2712.
[10] R.R. Hudgins, M.F. Jarrold, J. Am. Chem. Soc. 121 (1999) 3494.
[11] B.S. Kinnear, D.T. Kaleta, M.Kohtani, R.R. Hudgins, M.F. Jarrold, J. Am. Chem. Soc. 122 (2000) 9243.
[12] J. Woenckhaus, Y. Mao, M.F. Jarrold, J. Phys. Chem. B 101 (1997) 847.
[13] J.L. Fye, J. Woenckhaus, M.F. Jarrold, J. Am. Chem. Soc. 120 (1998) 1327.
[14] J.S. Klassen, A.T. Blades, P. Kebarle, J. Phys. Chem. 99 (1995) 15509.
[15] S.E. Rodriguez-Cruz, J.S. Klassen, E.R. Williams, J. Am. Soc. Mass Spectrom. 8 (1997) 565.
[16] S.-W. Lee, P. Freivogel, T. Schindler, J.L. Beauchamp, J. Am. Chem. Soc. 120 (1998) 11758.
[17] J. Woenckhaus, R.R. Hudgins, M.F. Jarrold, J. Am. Chem. Soc. 119 (1997) 9586.
[18] Y. Mao, M.A. Ratner, M.F. Jarrold, J. Am. Chem. Soc. 122 (2000) 2950.
[19] S.A. Shaffer, D.C. Prior, G.Anderson, H.R. Udseth, R.D. Smith, Anal. Chem. 70 (1998) 4111.
[20] SIMION, version 6.0, D. Dahl, Idaho National Engineering Laboratory, Idaho Falls, ID, 1995.
[21] A.V. Tolmachev, T. Kim, H.R. Udseth, R.D. Smith, T.H. Bailey, J.H. Futrell, Int. J. Mass Spectrom. 203 (2000) 31.
[22] P.R. Kemper, P. Weis, M.T. Bowers, Int. J. Mass Spectrom. Ion Processes 160 (1997) 17-37; P.R. Kemper, M.T. Bowers, J. Am. Soc. Mass Spectrom. 1 (1990) 197.
[23] E.A. Mason, E.W. McDaniel, Transport Properties of Ions in Gases, Wiley, New York, 1988.
[24] High injection energies were used to dissociate aggregates of singly protonated ions at the cell entrance.
[25] P.D. Schnier, W.D. Price, R.A. Jockusch, E.R. Williams, J. Am. Chem. Soc. 118 (1996) 7178.
[26] T. Wyttenbach, M.T. Bowers, J. Am. Soc. Mass Spectrom. 10 (1999) 9.
[27] E.F. Strittmatter, E.R. Williams, J. Phys. Chem. A 104 (2000) 6069.
[28] T. Wyttenbach, M.T. Bowers, unpublished results.
[29] Y. Mao, M.A. Ratner, M.F. Jarrold, J. Phys. Chem. B 103 (1999) 10017.
[30] H.W. Ellis, E.W. McDaniel, D.L. Albritton, L.A. Viehland, S.L. Lin, E.A. Mason, At. Data Nucl. Data Tables 22 (1978) 179.
[31] G.v. Helden, T. Wyttenbach, M.T. Bowers, Int. J. Mass Spectrom. Ion Processes 146 (1995) 349.
[32] A.E. Counterman, S.J. Valentine, C.A. Srebalus, S. C. Henderson, C.S. Hoaglund, D.E. Clemmer, J. Am. Soc. Mass Spectrom. 9 (1998) 743.
[33] S.-W. Lee, J.L. Beauchamp, J. Am. Soc. Mass Spectrom. 10 (1999) 347.
[34] I.R. Gatland, in Case Studies in Atomic Collision Physics, E.W. McDaniels, M.R.C. McDowell (Eds.), Vol. 4, North-Holland, Amsterdam, 1974, pp. 369–437.
[35] J. Gidden, T. Wyttenbach, P. Weis, A.T. Jackson, J.H. Scrivens, M.T. Bowers, J. Am. Chem. Soc. 121 (1999) 1421.